Monopulse Radial Line Slot Array Antenna Fed by a 3-D-Printed Cavity-Ended Modified Butler Matrix Based on Gap Waveguide at 94 GHz

Adrián Tamayo-Domínguez , *Student Member, IEEE*, José-Manuel Fernández-González , *Senior Member, IEEE*, and Manuel Sierra-Castañer , *Senior Member, IEEE*

***Abstract*— This article presents the design and fabrication of a monopulse radial line slot array (RLSA) antenna excited with a circular cavity connected to a modified Butler matrix at 94 GHz. The antenna consists of two pieces: the RLSA antenna implemented over a low loss dielectric substrate and a 3-D-printed Butler matrix based on gap waveguide. The interface between both parts is a circular cavity that couples two different modes into the RLSA through a coupling slot in the dielectric substrate. The coupled mode depends on the input excitation of the Butler matrix for the generation of simultaneous sum and difference radiation patterns. This interface is deeply detailed in this article, together with the design of the RLSA antenna and the integration of the full monopulse antenna. The measured S-parameters fit very well with simulations. The operation is inherently narrowband with a realized gain of 27.8 dBi at 94 GHz, a radiation efficiency of 70%, 0.3 dB axial ratio, and a maximum null relation between sum and difference patterns higher than 50 dB.**

***Index Terms*— Antennas, millimeter-wave antenna arrays, millimeter-wave waveguides, monopulse antennas, passive circuits, printing, radar antennas, slot arrays.**

I. Introduction

THE constant launching of artificial satellites into orbit and the increasing amount of space debris represent a serious problem for future space exploration missions and satellite telecommunications [1]–[3]. An effort is currently being made to investigate the systems capable of detecting small fragments of space debris to maintain control and minimize possible damage [4]–[8]. Space debris fragments of several centimeters in length are particularly harmful because of the difficulty in detecting them, according to the European Space Agency [9]. These fragments behave like bullets that can destroy complete satellite systems. These fragments can be detected and monitored using conventional radar techniques.

Since the creation of radar systems, there has been a need to know precisely the direction of arrival of detected targets and be able to track them. One of the most widely used systems since the 1960s has been the monopulse radar, which makes it possible to determine the direction by comparing the amplitude and phase of the signals received through the sum and difference beams, denoted as Σ and Δ from now on. The Σ configuration forms a high gain and low sidelobes beam and the Δ configuration generates a very deep null in boresight. The Σ beam is used to detect the target and the Δ beam provides the angle [10]. As the fragments to be detected are very small, antennas with a very high gain are required. To reduce the size of the antenna, this type of systems is being implemented at a frequency of 94 GHz.

Four-horn or phased array antennas have been typically used to implement monopulse antennas, but these are usually very voluminous and heavy or present a great circuit complexity [11]. In recent years, systems based on reflectors illuminated by 2×2 radiating elements with a comparator network [12]–[14] or linear slot arrays with large distribution networks [15]–[17] have been proposed. Some of them use rectangular waveguide technology, in which manufacturing can be critical when ensuring good electrical contact between parts in distribution networks. For this, manufacturing methods are highly expensive, such as silicon micromachining [12] or diffusion bonding [15]. To avoid these problems, the work in [16] uses gap waveguide technology [18] to prevent the need for good electrical contact between parts. Gap waveguide uses periodically arranged metal pins on which a metal plate is placed at a certain length. The size of the pins and the separation of the metal plate determine a bandgap in a range of frequencies. Thus, it is possible to avoid field leakage along distribution networks and other undesirable effects.

This work was supported in part by the Spanish Gov-ernment, Ministry of Economy, National Program of Research, Development and Innovation under the projects Enabling-5G "Enabling Innovative Radio Technologies for 5G Networks" under Project TEC2014–55735-C3-1-R, associated with the Formación de Personal Investigador (FPI) grant with reference BES-2015-075230, in part by the FUTURE-RADIO "Radio systems and technologies for high capacity terrestrial and satellite communications in an hyperconnected world" under Project TEC2017-85529-C3-1-R, and in part by the Madrid Regional Government under the project SPADERADAR "Space Debris Radar" under Project S2013/ICE-3000. *(Corresponding author: Adrián Tamayo-Domínguez.)*

The authors are with the Radiation Group, Department of Signals, Systems and Radiocommunications, Information Processing and Telecommunications Center (IPTC), Universidad Politécnica de Madrid, 28040 Madrid, Spain (e-mail: a.tamayo@upm.es; jmfdez@gr.ssr.upm.es; manuel.sierra@upm.es).

However, the complexity of manufacturing distribution networks with these periodic pin structures grows exponentially with the size (in wavelengths) and frequency, because of the small size of the pins required. Other works [13], [17] propose distribution networks based on substrate integrated waveguide (SIW), since the technology solves these problems of electrical contact with via holes at a much lower cost. The problem with these proposals is the high losses introduced by the dielectric in the distribution network. In general, the current systems are bulky, with high losses or with a high manufacturing cost.

In this work, we propose a monopulse antenna based on a radial line slot array (RLSA) fed by a Butler matrix that simultaneously generates the sum and difference patterns. RLSA antennas were investigated for the first time in 1985 for low-cost and high-efficiency telecommunication systems [19]. The Butler matrix used has paths with an effective length (in guide wavelengths) much smaller than other proposals and it is based on gap waveguide. To reduce the cost, it has been implemented by additive manufacturing, in particular, stereolithography (SLA) with subsequent copper plating. In addition to cost reduction, additive manufacturing allows to reduce considerably the weight of the pieces, since in this case it is formed by a UV-curable resin. Compared with the same piece made of aluminum, it is possible to reduce the weight by more than half. The versatility of 3-D printing when producing intricate parts means an increase in the degrees of freedom available both at the design stage and during fabrication. In addition, the emergence of affordable desktop SLA printers is a great opportunity to have a full in-house manufacturing system for prototyping. This manufacturing method applied to gap waveguide has given very good results in the *Ka*-band [20]–[22] and in the *W*-band [23].The RLSA antenna has been manufactured on a low loss dielectric substrate. There are works that use RLSA antennas to generate monopulse patterns at lower frequencies, but either use distribution networks based on microstrip [24] or the connectorization prevents them from being scaled to 94 GHz, due to lack of space [25].

A preliminary overview of the antenna design can be found in [26], where the schematic of the proposal and working principles are shown. This article is focused on the design of the RLSA antenna and the coupling between the Butler matrix and the RLSA. In particular, the critical parameters to be taken into account in the design of the coupling cavity, the integration of the complete antenna, and 3-D-printing manufacturing with measurement and validation of S-parameters and radiation patterns are deeply discussed. The detailed design of the Butler matrix, with experimental validation of the distribution network and each of its components can be found in [23]. From measurements, we estimate losses between 0.05 and 0.1 dB/cm and a total loss of 0.8 dB for the full Butler matrix.

The article is divided into six sections. Section II shows the antenna scheme. Section III shows the design of the RLSA antenna for simultaneous Σ and Δ patterns. Section IV presents the coupling circular cavity between the Butler matrix and the RLSA. The full integration of the monopulse antenna is validated in Section V. Finally, conclusions are drawn in Section VI.

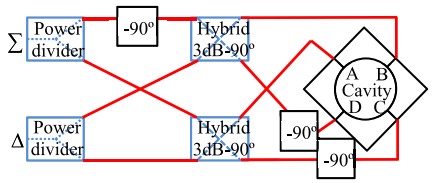

Fig. 1. Modified Butler matrix scheme and circular cavity.

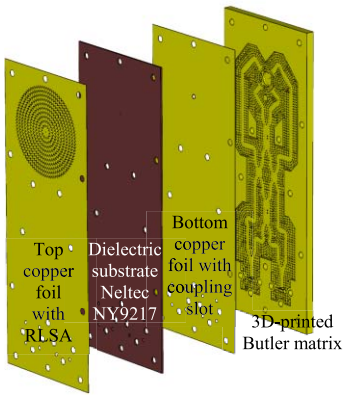

Fig. 2. Mounting scheme of the complete antenna.

II. Antenna Scheme

Due to the complexity of the design, the development and validation of the monopulse antenna has been carried out in two parts: the design of the RLSA antenna and the interface with the Butler matrix and the design of the Butler matrix itself [23].

A. Butler Matrix Scheme

In Fig. 1, a schematic of a modified Butler matrix whose four outputs are connected to a circular cavity is shown. This configuration produces a 90° sequential rotation at the inputs of the circular cavity (A, B, C, and D) when Σ port is excited and an equi-phase pattern when exciting the Δ port. Following the recommendations in [27], the required output phase scheme for monopulse operation is achieved.

B. RLSA Antenna Scheme

The complete antenna consists of two pieces: the 3-D-printed Butler matrix with the coupling cavity and the dielectric substrate with the RLSA in the top copper foil and the coupling slot in the bottom copper foil. Groove gap waveguide (GGW) [28] is used in the Butler matrix and circular cavity designs for low losses. The expanded view of the full monopulse antenna is illustrated in Fig. 2.

III. RLSA Design

RLSA antennas consist of two parallel plates with radiating slots distributed along the surface of at least one of them. The amplitude and phase distributions of the radial wavefront that propagates between both plates, and the arrangement of the slots determines the radiation performance. Monopulse operation can be achieved considering slots distributed in

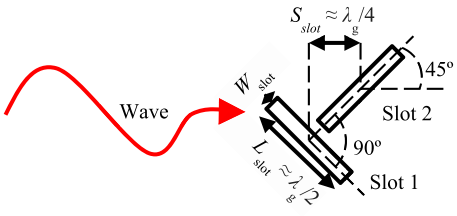

Fig. 3. Radiating element and parameters.

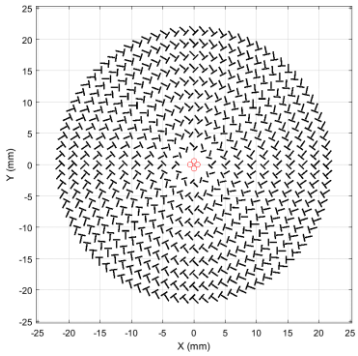

Fig. 4. Ten-ring RLSA antenna.

concentric rings. A uniform phase wavefront within the RLSA generates a Δ beam and a rotary phase wavefront (progressive linear phase) produces the Σ beam. For the detection of the angle of arrival, the value of θ is obtained by comparing the amplitude of both beams and the value of φ by comparing the phase. This monopulse operation is unusual since target detection is typically achieved by comparing the amplitude between a sum beam and two orthogonal difference beams. The monopulse antenna used in this design requires only one sum beam and one conical difference beam. Previous studies for monopulse antennas based on RLSA were presented in [24]. The antenna has T-shaped radiating elements with left-handed circular polarization. Fig. 3 illustrates the radiating element.

The RLSA antenna is implemented on a PTFE substrate Neltec NY9217 with a dielectric constant of 2.17, a loss tangent 0.0008 at 10 GHz, and a thickness of 0.762 mm. It is recommended to use dielectric constant values greater than 1.7 so that the separation between consecutive concentric rings is less than $0.75{\cdot}\lambda$ in free space for avoiding grating lobes.

The final distribution of the radiating elements in the ten-ring RLSA antenna is shown in Fig. 4. The diameter of the antenna is around 45 mm. The radiating elements have been optimized based on a global and a local algorithm [24], [29]. The algorithms maximize the relation between gain and spillover (power after the last ring of slots) for the Σ pattern. After the optimization, the position and length of the slots are obtained. The angle of the slots with respect to the radial wavefront is 45°, so that the excitation of the two slots of the radiant element is identical. All the design parameters of the slots are depicted in Fig. 5, which includes the distance from the center of the pair of slots of each ring, their length, and separation between them in millimeters and with respect

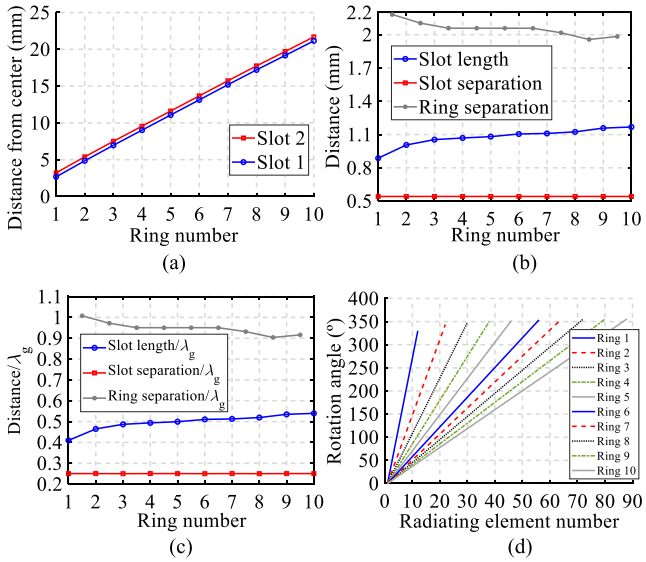

Fig. 5. Design parameters of the RLSA antenna: (a) distances of the slots to the center of the antenna, (b) slot length and separation between slot pairs and rings, (c) slot length and separation between slot pairs and rings normalized to the wavelength in the dielectric, and (d) rotation angle of the slots in each ring.

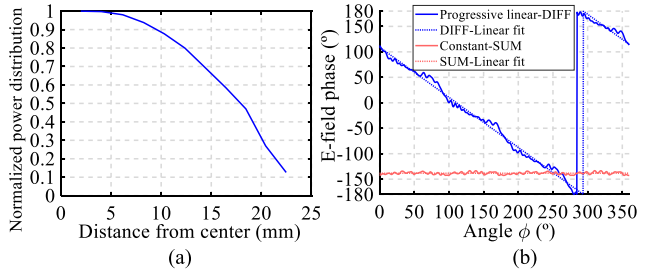

Fig. 6. Power and field values inside the RLSA: (a) power decay and (b) E-field phase in a circumference around the RLSA.

to the wavelength in the dielectric and the rotation angle of each radiating element in each ring. In Fig. 5(c), it can be seen that the length of the slots is around half a wavelength in the dielectric. This length starts in the first rings slightly below their resonant length to reduce the radiated power in the first stages. The length of the slots grows with each ring to achieve uniform illumination. In addition, the separation between the pair of slots of each radiating element is kept constant at a value of a quarter wavelength in the dielectric.

This provides two advantages: the two slots are excited orthogonally, so circular polarization is achieved, and the waves reflected by each slot cancel in the center of the antenna because they combine in counterphase, allowing a reduction of reflection. The RLSA antenna is designed for lossless exponential illumination, so that the real lossy substrate used in the antenna provides uniform illumination. The normalized power decay inside the lossless RLSA is shown in Fig. 6(a). In Fig. 6(b), the phase along a circumference centered on the origin of the RLSA results in a constant phase for the difference configuration and a progressive linear phase for the sum configuration.

The sum and difference radiation patterns at 94 GHz obtained with the RLSA antenna in Fig. 4 are shown

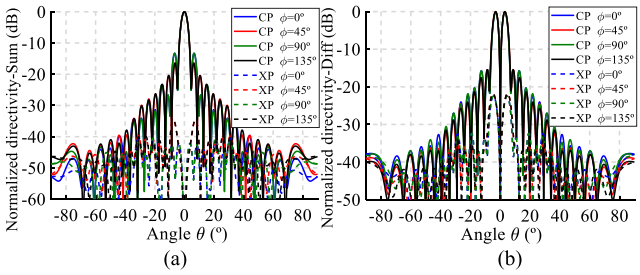

Fig. 7. Radiation diagrams at 94 GHz: (a) CP and XP sum patterns and (b) CP and XP difference patterns.

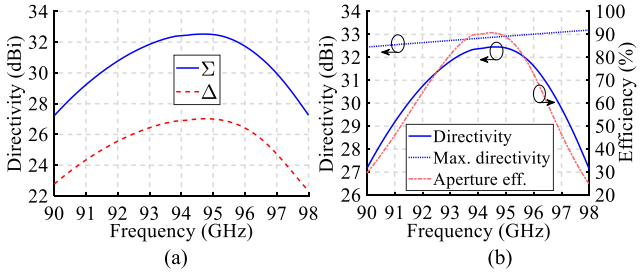

Fig. 8. (a) Directivity for the sum (Σ) and difference (Δ) patterns in the direction of maximum radiation. (b) Directivity and aperture efficiency for the sum pattern.

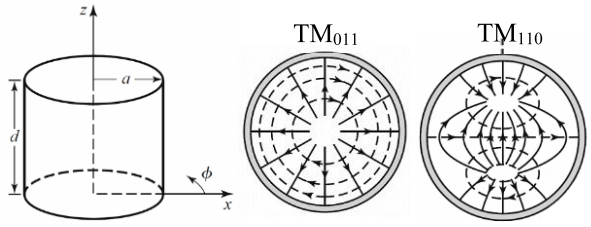

Fig. 9. Circular cavity parameters. Representation of the TM_{011} mode and a rotating TM_{110} mode. E-fields are shown as solid lines and H-fields dashed lines. Source [30].

in Fig. 7. The radiation diagrams include the copolar component (LHCP) and the cross-polar component (RHCP) for phi cuts of 0°, 45°, 90°, and 135°. The sidelobe level for the sum diagram is −13.5 and −16 dB for the difference diagram. The relation co-polar (CP)–cross-polar (XP) is 35 and 22 dB for the computed sum and difference patterns, respectively. The directivity as a function of the frequency for the direction of maximum radiation can be found in Fig. 8. Since the radiating elements used are narrowband in nature, the obtained aperture efficiency reaches values above 90% around 94 GHz, but falls rapidly to values of 30% at 90 and 98 GHz.

IV. RLSA to Circular Cavity Coupling

Once the RLSA antenna is designed, a circular cavity is chosen to generate the resonance of the TM_{0nm} and TM_{1nm} modes at the frequency of 94 GHz. As explained in Section III, the Δ configuration requires a uniform phase pattern inside the RLSA and the Σ pattern needs a rotary field distribution. To fit these requirements, the TM_{0nm} and TM_{1nm} modes in the circular cavity can be used. Fig. 9 shows the design

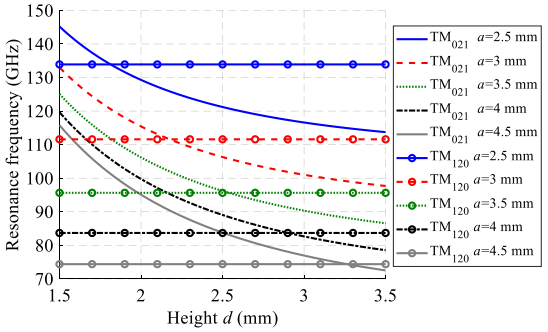

Fig. 10. Resonance frequencies as a function of radius and height of the circular cavity. Values for the TM_{120} and TM_{021} modes.

TABLE I
PARAMETER VALUES OF THE IDEAL CIRCULAR CAVITY

Modes	Radius	Height	Frequency
TM_{011} + TM_{110}	1.95 mm	2.05 mm	94 GHz
TM_{021} + TM_{120}	3.56 mm	2.58 mm	94 GHz
TM_{031} + TM_{130}	5.16 mm	3.03 mm	94 GHz

parameters of the circular cavity and a scheme of the fields inside the cavity. Expression (1) shows the classic formula for the resonance frequency of modes inside a circular cavity [30]

$$f_{nml} = \frac{c}{2\pi\sqrt{\mu_r \varepsilon_r}} \sqrt{\left(\frac{p_{nm}}{a}\right)^2 + \left(\frac{l\pi}{d}\right)^2}. \quad (1)$$

The parameter p_{nm} represents the mth root of the Bessel function of order n. With these values, the resonance frequencies of the modes TM_{011}, TM_{021}, TM_{031}, TM_{110}, TM_{120}, and TM_{130} can be calculated as a function of the radius a and height d of the circular cavity. The variation in resonance frequencies of the TM_{021} and TM_{120} modes is shown in Fig. 10 as a function of d for different values of a. Since the resonance frequency of modes TM_{1m0} does not change when the height varies, it is easy to find the radius and height values where both modes TM_{0m1} and TM_{1m0} resonate at 94 GHz. Applying (2) and (3), the dimensions of the hollow circular cavity are obtained to excite the desired modes. The resulting dimensions for the selected modes in the ideal circular cavity are listed in Table I. Expression (2) for calculating the radius a depends only on the resonance frequency f and the chosen mode TM_{1m0} (p_{1m}). Expression (3) requires the previously calculated radius a, the resonance frequency f, and the chosen mode TM_{0m1} (p_{0m} and $l = 1$) for the calculation of the height d. After preliminary calculations of the dimensions of an ideal circular cavity, we applied the values of radius and height obtained to a circular cavity based on gap waveguide. The dimensions of the pins are the same as those used in the design of the Butler matrix [23], with a diameter of 0.5 mm, a height of 0.9 mm, and a periodicity of 1.2 mm with 0.5 mm thick air gap. The cylindrical wall of the cavity is replaced by four concentric rows of pins to ensure good field insulation inside the cavity. With this modification of the structure, it is necessary to readjust the dimensions to generate the desired modes at 94 GHz. Starting from the ideal cavity, three different

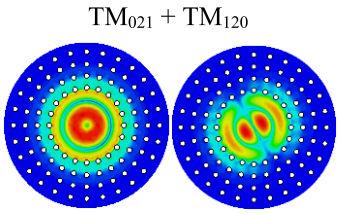

Fig. 11. Amplitude of the E-field for the TM_{021} and TM_{120} modes at 94 GHz.

TABLE II
PARAMETER VALUES OF THE GGW CIRCULAR CAVITY

Modes	Radius	Height	Prev. mode	Next mode
$TM_{011} + TM_{110}$	1.88 mm	2.08 mm	87 GHz	97 GHz
$TM_{021} + TM_{120}$	3.51 mm	2.60 mm	91.3 GHz	100.7 GHz
$TM_{031} + TM_{130}$	5.12 mm	3.04 mm	93.5 GHz	94.7 GHz

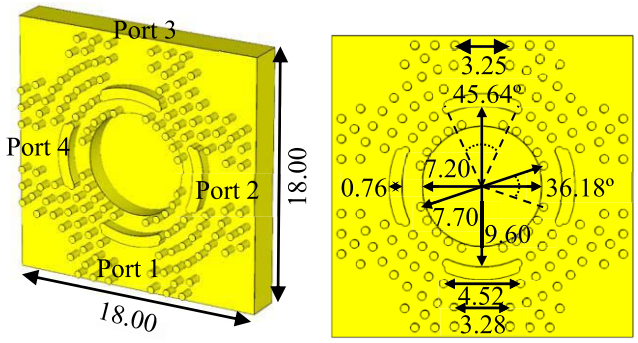

Fig. 12. Top view of the designed gap waveguide circular cavity. Length values are in millimeters.

cavities have been designed for the three configurations of Table I

$$a = \frac{c \cdot p_{1m}}{2\pi \cdot f} \tag{2}$$

$$d = \frac{c \cdot l}{2\sqrt{f^2 - \left(\frac{c \cdot p_{0m}}{2\pi \cdot a}\right)^2}}. \tag{3}$$

The adjusted dimensions of the GGW circular cavities are shown in Table II, together with the frequencies of previous and next undesired resonant modes. The final selected modes in Fig. 11 are TM_{021} and TM_{120} because the associated cavity radius is large enough to allow an ample access of four GGW inputs and the adjacent unwanted modes are several gigahertz away from 94 GHz.

A slot centered in the ground plane of the RLSA is used for coupling the field from the circular cavity to the RLSA antenna. In a first approximation, the design and optimization of this stage is done considering an infinite parallel plate waveguide (PPWG) instead of the real RLSA antenna. This allows us to drastically reduce the computing time taking into account that the effect of the radiating slots on the matching between the four GGW inputs and the central slot coupled to the RLSA will be negligible. The designed cavity coupled to the PPWG is shown in Figs. 12 and 13.

The coupling slot between the circular cavity and the PPWG in the final design is not circular, but wavy. This is due to the

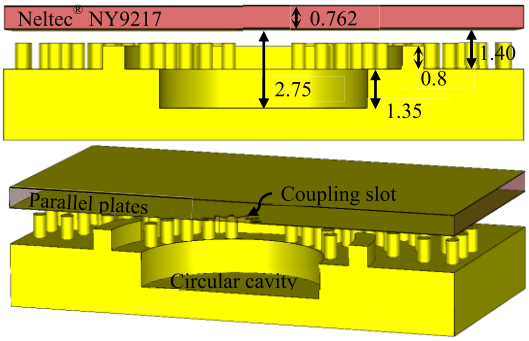

Fig. 13. Lateral cross section of the circular cavity coupled to the dielectric-filled PPWG. Length values are in millimeters.

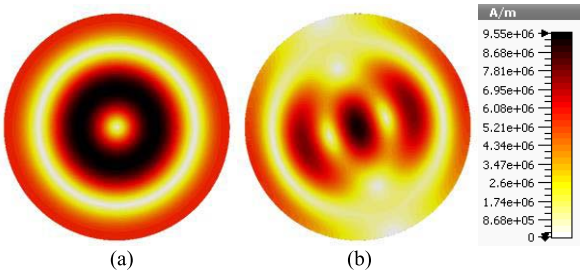

Fig. 14. Representation of the surface current at the top face of the ideal circular cavity for (a) TM_{120} and (b) TM_{021} modes at 94 GHz.

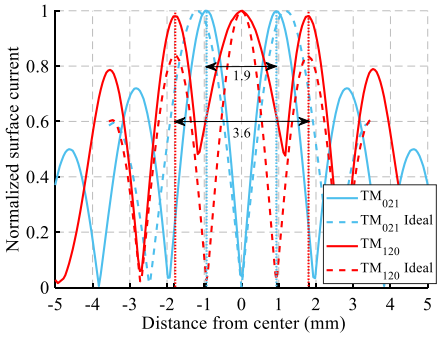

Fig. 15. Radial normalized surface current for the TM_{120} and TM_{021} modes at 94 GHz in the top face of the ideal cavity and in the designed gap waveguide cavity in Fig. 13.

shape of the surface currents in the upper face of the circular cavity. Since the slot must simultaneously couple modes TM_{021} and TM_{120}, the radius of this slot must approximately coincide with the maximum of the surface current in the radial direction. Fig. 14 depicts the amplitude of the current in the upper face of the ideal circular cavity for both modes, taking into account that the amplitude of the current for mode TM_{120} [Fig. 14(b)] also has a rotary pattern with sum mode excitation. The amplitude of these normalized currents in a radial cut is represented in Fig. 15. This graph includes the currents for both the ideal circular cavity and the designed GGW cavity of Figs. 12 and 13. In Fig. 15, the distance between current peaks is 1.9 and 3.6 mm, respectively, for the TM_{021} and TM_{120} modes. This difference prevents an efficient simultaneous coupling of both the modes using a circular slot.

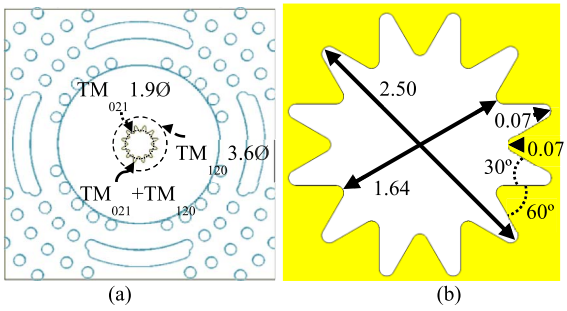

Fig. 16. Coupling slot from the circular cavity to the PPWG. (a) Representation of the circular slots for good matching of the TM_{120} mode (dashed curve), the TM_{021} mode (dotted curve), and both of them (solid curve). (b) Design parameters of the final wavy slot for simultaneous matching of the TM_{120} and TM_{021} modes at 94 GHz.

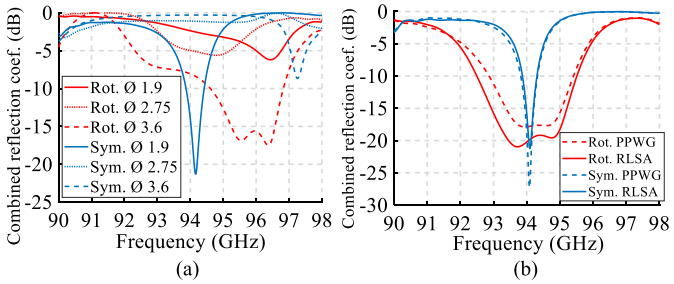

Fig. 17. Matching of the rotary (TM_{120}) mode and symmetric (TM_{021}) mode for various shapes of the coupling slot. (a) Circular slots with various diameters and (b) final wavy slot.

Fig. 16(a) shows the structure of the gap waveguide cavity with different shapes and sizes of coupling slot to the PPWG. The two circular shapes correspond to the slots with the diameter of 1.9 mm and 3.6 mm, coincident with the current peaks shown in Fig. 15. A wavy slot is superposed over them to find an efficient simultaneous coupling. The design parameters of this wavy slot are presented in detail in Fig. 16(b).

The S-parameters of the cavity with four ports are shown in Fig. 17. The results for circular coupling slots of 1.9 and 3.6 mm diameter can be seen in Fig. 17(a), together with an additional result for an average diameter of 2.75 mm. As expected, matching at 94 GHz using a 1.9 mm slot is acceptable for the symmetrical mode (TM_{021}), but very bad for the rotary mode (TM_{120}), and vice versa when using the 3.6 mm slot. With the average diameter slot, a bad matching is achieved in both the cases. However, when using the wavy slot in Fig. 16(b), it is possible to achieve a good matching for both the configurations simultaneously. The final results with this wavy slot are shown in Fig. 17(b), which also compares the reflection coefficient of the cavity coupled to the PPWG without RLSA and with the integrated RLSA. The only effect of introducing the RLSA is an improvement of the reflection level for the sum configuration (rotary mode).

It should be noted that the results obtained are inherently narrowband due to the nature of the resonant cavity. In particular, during the process of optimization of the cavity and the coupling slot, it has been intended to maintain a greater bandwidth for the sum mode at the cost of narrowing

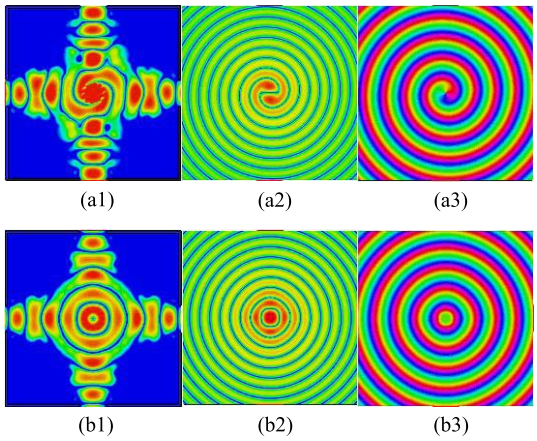

Fig. 18. (a1)–(a3) Field representation of rotary mode and (b1)–(b3) symmetric mode. (a1)–(b1) Amplitude of the electric fields in the circular cavity, (a2)–(b2) amplitude of the electric fields coupled to PPWG, and (a3)–(b3) phase of the electric field coupled to PPWG.

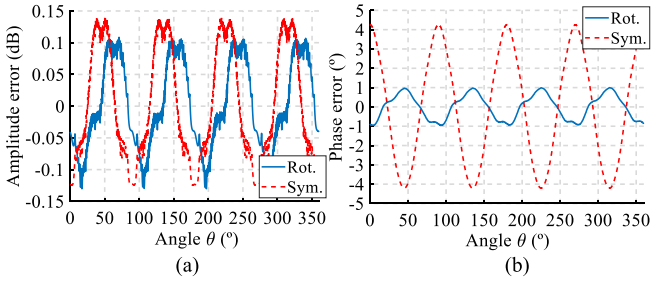

Fig. 19. (a) Amplitude and (b) phase errors of the z-component of the E-field for the rotary and symmetric modes inside the PPWG for wavefronts at a radius $R = 6$ mm.

the band of the difference mode. The idea is to minimize the risk of mismatch losses in the sum mode if there is a frequency deviation of the response in the manufactured prototype. A drop in gain along the boresight direction means a reduction of the system's performance in detecting targets of a certain size at a given distance.

Fig. 18 illustrates the field distributions in two different cross sections of the cavity to PPWG design: one cross section in a plane inside the resonant cavity immediately below the coupling slot and the other in the central plane of the PPWG. The rotating pattern is presented in Fig. 18(a1)–(a3) and the radially uniform pattern is depicted in Fig. 18(b1)–(b3): (a1) and (b1) show the amplitude of the field inside the cavity, (a2) and (b2) the amplitude in the central plane of the PPWG, and (a3) and (b3) the phase. For the rotating mode, the four ports that excite the cavity have a sequential phase shift of 90° and the field inside the PPWG exhibits a circular spiral pattern. For the radially uniform mode, the input ports are excited with the same phase, resulting in the coupling of a radially symmetrical field inside the PPWG.

The amplitude and phase errors in a circumference with radius $R = 6$ mm are represented in Fig. 19. The maximum amplitude and phase errors achieved in the final design are summarized in Table III. The errors obtained are very small due to the high radial symmetry of the coupling cavity.

TABLE III
PHASE AND AMPLITUDE ERRORS FOR E_z IN THE PPWG FOR WAVEFRONTS AT $R = 6$ mm

Type of field	*Phase error (°)*	*Amplitude error (dB)*
ROTARY	1.0	0.10
SYMMETRIC	4.2	0.14

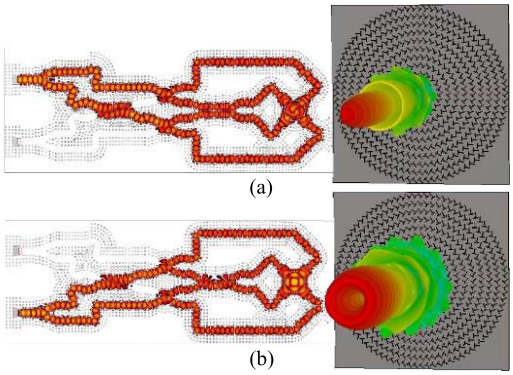

Fig. 20. Operation of the Butler matrix together with the radiation diagrams obtained for (a) Σ configuration and (b) Δ configuration.

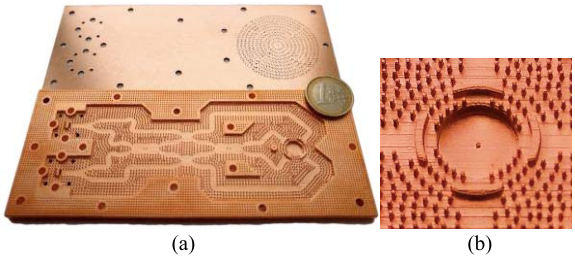

Fig. 21. (a) Picture of the manufactured monopulse antenna before assembling and (b) detail of the circular cavity with alignment hole.

V. INTEGRATION OF THE FULL MONOPULSE ANTENNA

The results of the integration of the Butler matrix coupled to the RLSA via the circular cavity are detailed in this section. Fig. 20 illustrates the monopulse operation of the complete antenna. The electric field distribution inside the Butler matrix for Σ port excitation is shown in Fig. 20(a). This distribution imposes phase conditions in the coupling cavity that induce the rotation of the field. The result is the pencil beam shown on the right. When the structure is fed through the Δ port, the field distribution shown in Fig. 20(b) is obtained. In this case, the phase conditions imposed by the Butler matrix in the cavity generate a radially uniform mode. The coupling of this mode within the RLSA results in a conical radiation pattern with a pronounced null in boresight. The combined operation of both the sum and difference diagrams allows the monopulse function. The low amplitude and phase errors of the wavefronts in the PPWG are reflected in the high rotational symmetry of the obtained radiation diagrams. The final prototype of the manufactured monopulse antenna is shown in Fig. 21.

The dimensions of the assembled prototype are $150 \times 60 \times 4.7$ mm. One of the critical parts of manufacturing is to get a good alignment between the two parts that form the antenna. The only alignment requirement that must be met is that the center of the RLSA on the PCB matches the center of the circular cavity of the 3-D printed part. To achieve this, a pair of holes have been made in the PCB and the circular cavity to align with a 0.3 mm diameter pin traversing the two pieces from side to side. For manufacturing reasons, the hole in the PCB has been defined with a diameter of 0.35 mm to maintain a clearance that allows the pin to slide. Similarly, the hole in the cavity has been defined with a diameter of 0.45 mm, since a smaller hole is likely to close completely during the 3-D printing process and subsequent copper plating. An image of the cavity with the alignment hole is shown in Fig. 21(b). A detailed view of the coupling slot and the manufactured radiating elements is shown in Fig. 22(a) and (b). The coupling slot presents the wavy pattern described in Fig. 16(b) and a central hole of 0.35 mm in diameter to align the PCB with the 3-D printed plate. The material used to manufacture this prototype is Accura SL 5530 [31] with a layer thickness of 0.05 mm. This is achieved by photopolymerizing the UV-sensitive resin layer by layer with a laser beam of 0.075 mm $\pm$ 0.015 mm in diameter. For this resolution, there is a maximum part size of $250 \times 250 \times 250$ mm^3, and a minimum geometry size of 0.13 mm in the XY plane and 0.4 mm in the Z plane. The tolerances are typically better than $\pm$0.05 mm in the XY plane and better than $\pm$0.13 mm in the Z plane, with an additional 0.001 mm/mm in both the cases, although these tolerances depend on the shape and dimensions of the part. Of course, there are other materials available and different layer resolutions depending on manufacturing requirements. These characteristics of the SLA process are sufficient to achieve good results even in prototypes operating in the W-band, as demonstrated in this section. A photograph of the assembly for measurement of S-parameters and setup in the anechoic chamber are included in Fig. 22(c) and (d).

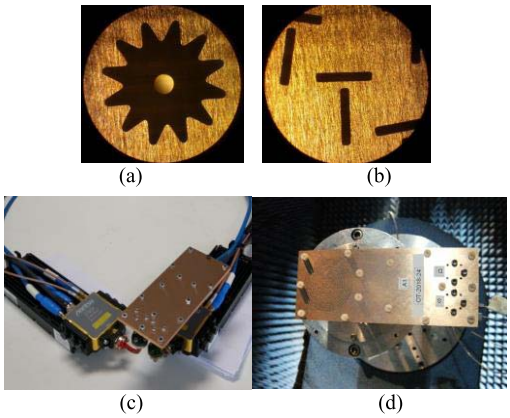

Fig. 22. Microphotographs of the PCB: (a) wavy coupling slot and (b) T-shaped radiating elements. The central hole in (a) has a diameter of 0.35 mm for alignment. (c) Setup for S-parameters measurement. (d) Monopulse RLSA antenna in anechoic chamber for measurement.

The measurements are represented in Fig. 23 together with the simulated S-parameters of the complete structure. The bandwidth difference of the two patterns is clearly observed, with 0.8 GHz at -10 dB for the difference (Δ) pattern

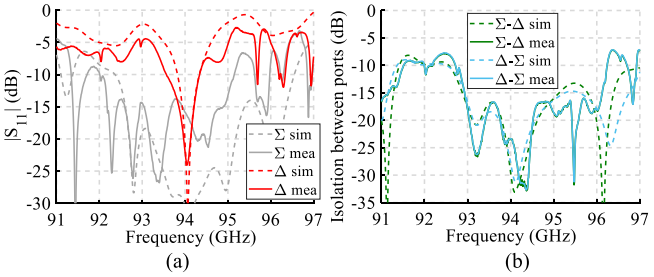

Fig. 23. Simulated and measured S-parameters: (a) reflection coefficients and (b) isolation coefficients.

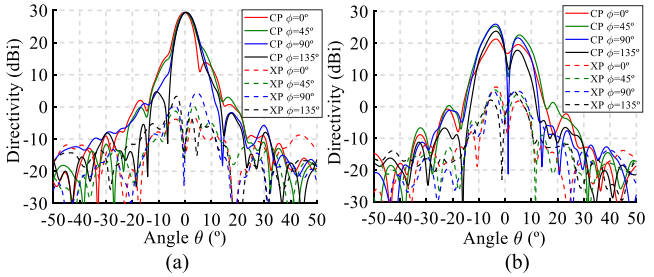

Fig. 24. Measured Σ (a) and Δ (b) patterns (directivity—LHCP) for different azimuth angles at 94 GHz.

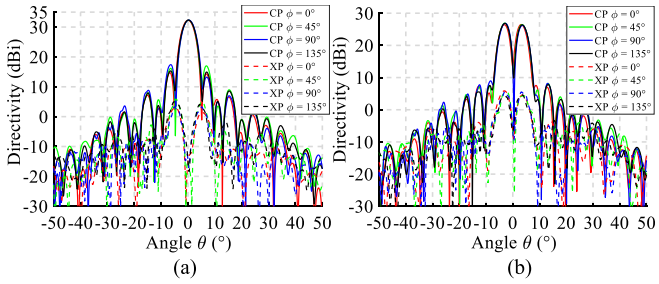

Fig. 25. Simulated Σ (a) and Δ (b) patterns (directivity—LHCP) for different azimuth angles at 94 GHz.

and 4 GHz for the sum (Σ) pattern. Both the reflection coefficients fit well with the simulations. The measured and simulated isolation between ports is practically identical, with values below −15 dB between 93 and 95 GHz and a value around −25 dB at the central frequency. This validates additive manufacturing at frequencies close to 100 GHz with a high degree of fidelity to the ideal model.

The measurements of the radiation patterns of the monopulse antenna were made in the spherical system of the anechoic chamber LEHA-UPM. Fig. 24 depicts the measured radiation patterns of the Σ [Fig. 24(a)] and Δ [Fig. 24(b)] configurations at 94 GHz for different azimuth angles, along with the cross-polar component. For comparison, the results obtained from the simulations are represented in Fig. 25 for the two patterns and the same cuts in φ angle.

In simulation, the high symmetry of the coupling cavity to the RLSA generates very stable radiation patterns in φ angle, since it results in very small phase and amplitude errors inside the RLSA. There is some small secondary lobe imbalance produced by small phase imbalances in the Butler matrix

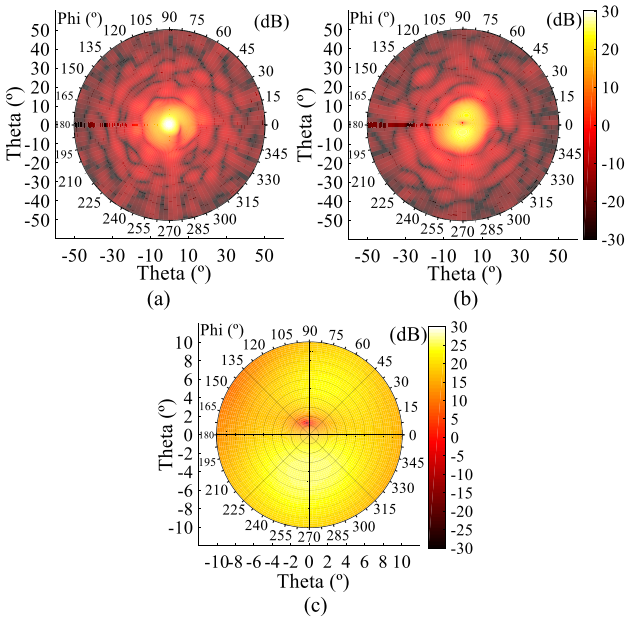

Fig. 26. 2-D plots of the measured radiation diagrams: (a) sum pattern, (b) difference pattern, and (c) zoom of the difference pattern for better visualization of the deep null.

outputs that excite the cavity. These phase imbalances are difficult to correct, as the external paths are longer than the internal ones, so the Butler matrix in not fully symmetrical. However, the measured radiation patterns show asymmetries due to amplitude and phase errors caused by manufacturing tolerances, assembly, and variations in the dielectric substrate properties. The simulated sum diagram has a maximum directivity of 32.3 dBi, while in measure the directivity drops almost 3 dB to a value of 29.35 dBi. The secondary lobe level for the sum beam is better than −15 dB in simulation, but in measurement the nulls of the secondary lobes are filled. The reduction of directivity and nulls filling is due to an excitation of the rings with a nonuniform phase produced by a deviation of the dielectric constant of the substrate. Also, a marked asymmetry is observed in the cuts of the difference diagram, in which the null presents a value of −21.2 dBi and a deviation of 1.5° with respect to broadside.

For a better perspective of the radiation patterns measured on the sphere, 2-D radiation diagrams are represented in Fig. 26. With this representation, the produced asymmetries and the deviation of the null of radiation of the difference diagram can be better observed. The 2-D measurements are represented in a range of angles from −50° to 50° in theta and from 0° to 360° in phi for the sum [Fig. 26(a)] and difference [Fig. 26(b)] diagrams. For a clearer view of the null, a zoom of the difference diagram is included for a range in theta of −5° to 5° in Fig. 26(c). The 2-D measurements also correspond to the results for 94 GHz.

The measurements of directivity and realized gain variation of the sum beam with frequency are shown in Fig. 27. Fig. 27(b) includes the simulated directivity taking into account the cumulative errors and deviations. Considering an error of 30 μm rms in the slots' length (value provided by

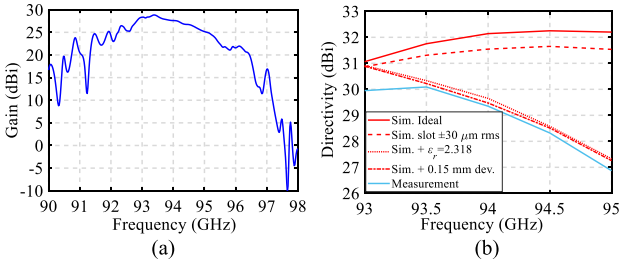

Fig. 27. (a) Measured realized gain between 90 and 98 GHz and (b) measured and simulated directivity between 93 and 95 GHz.

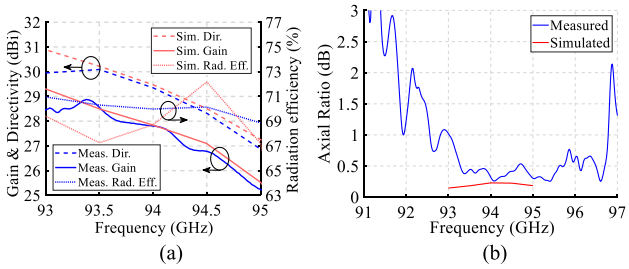

Fig. 28. (a) Comparison between measurements and final simulated directivity, realized gain, and radiation efficiency. (b) Measured and simulated axial ratio versus frequency.

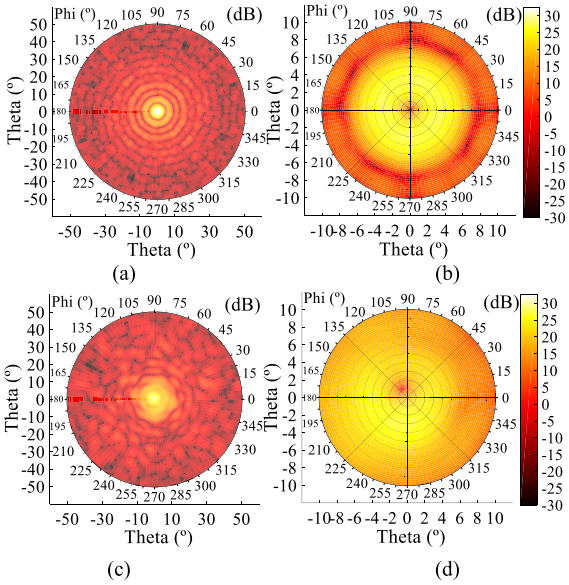

Fig. 29. 2-D radiation diagrams for ideal and adjusted simulations: (a) sum beams for ideal simulation and (c) simulation with error in slots length, dielectric constant deviation, and 0.15 mm misalignment. (b) Difference beams for ideal simulation and (d) simulation with error in slots length, dielectric constant deviation, and 0.15 mm misalignment.

our manufacturer), a deviation of the dielectric constant of the substrate from 2.17 to 2.318, and a misalignment between the Butler matrix and RLSA of 0.15 mm (as explained in Fig. 29), the simulated directivity is very close to the measured one. A maximum realized gain of 28.86 dBi is observed at 93.4 GHz with an approximately constant decrease to 95 GHz. The realized gain value at 94 GHz is 27.8 dBi. Fig. 28(a) compares the final measurements and simulated directivity, realized gain, and radiation efficiency, which is about 70% between 93 and 95 GHz in simulation and measurement.

A comparison of the axial ratio of the measured and simulated sum beam as a function of frequency can be seen in Fig. 28(b). The measured results show a very good circular polarization, with an axial ratio below 0.5 dB between 93.5 and 95.5 GHz. The minimum of 0.26 dB is at 94.08 GHz, very close to the simulated values around 0.2 and 0.3 dB.

To finalize the analysis of the results obtained, a study of tolerances in the alignment between the two parts of the antenna has been carried out. A misalignment of 0.15 mm is necessary to obtain the measured deviation of 1.5° from boresight of the null in the difference diagram. For the ideal case in Fig. 29(a) and (b), the sum diagram and the difference diagram are well-centered, with a high rotational symmetry. In the sum diagram, the secondary lobes appear well-defined with deep nulls between them. When applying the 0.15 mm mismatch in Fig. 29(c) and (d), together with the other errors and deviations analyzed in Fig. 27(b), the symmetry is broken and the secondary lobes are blurred in the same way as in the 2-D representation of the measurements in Fig. 26. In addition, the null of radiation of the difference diagram has deviated to 1.5°. A clear unbalance of the level of the conical beam of the difference diagram is observed, with a maximum of 28.5 dB and a minimum of 22.5 dB in the cut $\varphi = 75°$. However, taking into account the complexity of the prototype and the tolerances of the manufacturing processes, we consider that the result obtained is remarkable.

A comparison with other works is conducted in Table IV. The elements included in the comparison are the type of comparator and antenna used, the number of pieces, parts or layers that compose the antenna, the type of transmission line, the manufacturing technology used, the size, characterization of S-parameters, and antenna performance. The proposals with magic tee present acceptable performance in all aspects, but this type of structures typically requires a multi-level distribution network with several layers. The Butler matrices can be designed on a single level, reducing manufacturing complexity, alignment errors, and cost. In addition, the proposals with magic tee [12], [15]–[16] are made of metal with expensive manufacturing processes. The proposal in [16] takes advantage of the gap waveguide for the distribution network. The design uses multiple layers using computer numerical control (CNC) milling for the manufacturing process, which is much more expensive than additive manufacturing. The rest of the proposals in Table IV uses the Butler matrices. The design of most of them is based on SIW manufactured using PCB technology [13]–[17]. The presence of the dielectric substrate results in an antenna efficiency below 20%. In [14], the Butler matrix is based on the rectangular waveguide manufactured with CNC milling at 94 GHz. The feeding network illuminates a Cassegrain reflector system that must be very well aligned. With respect to the bandwidth, the magic tee designs typically achieve relative bandwidths of 20% with an isolation of more than 30 dB. The Butler-matrix-based designs can reach bands above 2% and isolation above 20 dB. Only full metal proposals without reflector components present an antenna efficiency above 60%.

TABLE IV
COMPARISON WITH PREVIOUS WORKS

Ref.	Feeding network[1]			Physical features		Scattering Parameters[2]				Antenna performance[3]					
	Comparator/ Antenna	Type	Manuf.	Size ($x\lambda_0$)	Number Pieces	f_0 (GHz)	BW (%)	VSWR	Iso. (dB)	G_Σ (dBi)	XP_Σ (dBi)	ND_Δ (dB)	SLL_Σ (dB)	Pol./AR (dB)	η (%)
[12]	MT/2x2-SHA	RW	SM	12x11.3x0.8	6	90.5	15	2	45*	14.2	n. a.	49	-10	Linear	69
[13]	BM/Reflector	SIW	PCB/CNC	43.9x43.9x17.2	2	94	1.7	2	n. a.	35.6	-21.3	25	-13	RHCP/1.5	19.1[a]
[14]	BM/Cassegrain	RW	CNC	42.3x42.3x14.6	5	94	4.3	1.4	21	35.1	-23	40	-17	RHCP/1.2	18.3[a]
[15]	MT/Array	RW	DB	13.3x13.3x1.5	29	78.5	21.9	2	n. a.	32.6	n. a.	53	-13	Linear	83
[16]	MT/Array	GW	CNC	17.4x17.4x2.9	4	95	21	2	50	30.5	-27	40	-13	Linear	60
[17]	BM/Array	SIW	PCB	41x39.4x0.16	1	94.5	1.6	1.4	n. a.	25.8	n. a.	45.8	-10	Linear	15.2
Our work	BM/RLSA	GW	3D-SLA	47x18.8x1.5	2	94	0.83	2	20	27.8	-30.8	50	-14	LHCP/0.5	70

[1] Feeding network: MT: Magic Tee, BM: Butler Matrix, SHA: Stepped Horn Antenna, RLSA: Radial Line Slot Array. Transmission line: RW: Rectangular Waveguide, GW: Gap Waveguide, SIW: Substrate Integrated Waveguide. Manufacturing technology: DB: Diffusion Bonding, SM: Silicon Micromachining, CNC: Computer Numerical Controlled Milling, PCB: Printed Board Circuit, 3D-SLA: Stereolithography (3D-Printing).
[2] Scattering Parameters: f_0: central frequency, BW: relative bandwidth, Iso.: Isolation between input ports.
[3] Antenna performance: G_Σ: Gain of the SUM beam, XP_Σ: Cross-polar level of the SUM beam relative to co-polar, ND_Δ: Null depth of the DIFF beam relative to the SUM beam, SLL_Σ: Side Lobe Level of the SUM beam, Pol./AR: Polarization and axial ratio if circular polarized, η: radiation efficiency.
* Simulated value, [a] Total efficiency (factor of aperture and radiation efficiencies)

The prototype presented in this work takes advantage of the high precision of the current SLA 3-D printing techniques with copper plating. The 0.83% bandwidth is limited by the difference pattern due to the inherently narrowband circular cavity used. This design consideration was chosen considering that the working band around 94 GHz is very narrow (±200 MHz, 0.4%) for a monopulse radar, so the values obtained are good enough for the operation of the system. The isolation is better than 20 dB and the antenna efficiency is 70%, better than most of the works. The maximum null relation is about 50 dB and the axial ratio is better than 0.5 dB LHCP. These results highlight over the other works in the comparison.

VI. CONCLUSION

The proposed *W*-band monopulse antenna is based on an RLSA antenna fed by a circular cavity connected to a two-input Butler matrix to simultaneously generate the sum and difference patterns. The prototype design is oriented to manufacturing with PCB technology for the RLSA and additive manufacturing for the feeding structure. The use of 3-D-printing instead of CNC for the feeding network has resulted in a significant reduction in the cost of prototyping. The results of the complete antenna prototype show a good behavior of the sum and difference patterns with a measured directivity of almost 30 dBi, an antenna efficiency of 70% for the sum beam, and a 50 dB deep null at 1.5° from broadside for the difference beam. The achieved axial ratio is also very low about 0.5 dB in a 2 GHz band for LHCP. The effective fractional bandwidth is 0.87% due to the limitations of the difference configuration and the inherently narrowband behavior of the coupling circular cavity. Despite this, the measurements fit very well with simulations, thanks to the high manufacturing accuracy.

REFERENCES

[1] H. Lamb, "Space agencies turn focus on small space debris," *Eng. Technol.*, vol. 13, no. 1, pp. 48–49, Feb. 2018.

[2] S. Fukushige *et al.*, "Solar-array arcing due to plasma created by space-debris impact," *IEEE Trans. Plasma Sci.*, vol. 36, no. 5, pp. 2434–2439, Oct. 2008.

[3] M. Torky, A. E. Hassanein, A. H. El Fiky, and Y. Alsbou, "Analyzing space debris flux and predicting satellites collision probability in LEO orbits based on Petri nets," *IEEE Access*, vol. 7, pp. 83461–83473, 2019.

[4] S. Tao, S. Xiuming, and C. Jing, "Three-dimensional imaging of spinning space debris based on the narrow-band radar," *IEEE Geosci. Remote Sens. Lett.*, vol. 11, no. 6, pp. 1041–1045, Jun. 2014.

[5] Y. Ning, F. Zhou, X. Bai, and L. Liu, "A method for 3-D ISAR imaging of space debris," *IEEE Trans. Aerosp. Electron. Syst.*, vol. 55, no. 2, pp. 864–876, Apr. 2019.

[6] D. Mo, N. Wang, G. Li, R. Wang, and Y. Wu, "3-D inverse synthetic aperture ladar imaging and scaling of space debris based on the fractional Fourier transform," *IEEE Geosci. Remote Sens. Lett.*, vol. 16, no. 2, pp. 236–240, Feb. 2019.

[7] X. Yang, Y. Pi, T. Liu, and H. Wang, "Three-dimensional imaging of space debris with space-based terahertz radar," *IEEE Sensors J.*, vol. 18, no. 3, pp. 1063–1072, Feb. 2018.

[8] M. C. Pasqual and K. L. Cahoy, "Active polarimetric measurements for identification and characterization of space debris," *IEEE Trans. Aerosp. Electron. Syst.*, vol. 53, no. 6, pp. 2706–2717, Dec. 2017.

[9] *Serving European Cooperation and Innovation. European Space Agency*, The ESA Effect, Paris, France, 2014.

[10] M. I. Skolnik, *Radar Handbook*. New York, NY, USA: McGraw-Hill, 1970.

[11] S. M. Sherman and D. K. Barton, *Monopulse Principles and Techniques*. Norwood, MA, USA: Artech House, 2011.

[12] F. Zhao, Y. J. Cheng, P. F. Kou, and S. S. Yao, "A wideband low-profile monopulse feeder based on silicon micromachining technology for W-band high-resolution system," *IEEE Antennas Wireless Propag. Lett.*, vol. 18, no. 8, pp. 1676–1680, Aug. 2019.

[13] P. F. Kou and Y. J. Cheng, "A dual circular-polarized extremely thin monopulse feeder at W-band for prime focus reflector antenna," *IEEE Antennas Wireless Propag. Lett.*, vol. 18, no. 2, pp. 231–235, Feb. 2019.

[14] P. Zheng, G. Q. Zhao, S. H. Xu, F. Yang, and H. J. Sun, "Design of a W-band full-polarization monopulse cassegrain antenna," *IEEE Antennas Wireless Propag. Lett.*, vol. 16, pp. 99–103, 2017.

[15] X. Xu, J. Hirokawa, and M. Ando, "An E-band slotted waveguide monopulse array antenna with corporate-feed using diffusion bonding of laminated plates," in *Proc. ISAP*, Oct. 2016, pp. 308–309.

[16] A. Vosoogh, A. Haddadi, A. U. Zaman, J. Yang, H. Zirath, and A. A. Kishk, "*W*-band low-profile monopulse slot array antenna based on gap waveguide corporate-feed network," *IEEE Trans. Antennas Propag.*, vol. 66, no. 12, pp. 6997–7009, Dec. 2018.

[17] Y. J. Cheng, W. Hong, and K. Wu, "94 GHz substrate integrated monopulse antenna array," *IEEE Trans. Antennas Propag.*, vol. 60, no. 1, pp. 121–129, Jan. 2012.

[18] P.-S. Kildal, "Three metamaterial-based gap waveguides between parallel metal plates for mm/submm waves," in *Proc. EuCAP*, Mar. 2009, pp. 28–38.

[19] M. Ando, K. Sakurai, N. Goto, K. Arimura, and Y. Ito, "A radial line slot antenna for 12 GHz satellite TV reception," *IEEE Trans. Antennas Propag.*, vol. 33, no. 12, pp. 1347–1353, Dec. 1985.

[20] A. Tamayo-Dominguez, J.-M. Fernandez-Gonzalez, and M. Sierra-Perez, "Groove gap waveguide in 3-D printed technology for low loss, weight, and cost distribution networks," *IEEE Trans. Microw. Theory Techn.*, vol. 65, no. 11, pp. 4138–4147, Nov. 2017.
[21] A. Tamayo-Dominguez, J.-M. Fernandez-Gonzalez, and M. Sierra-Perez, "Metal-coated 3D-printed waveguide devices for mm-wave applications [Application Notes]," *IEEE Microw. Mag.*, vol. 20, no. 9, pp. 18–31, Sep. 2019.
[22] M. Ferrando-Rocher, J. I. Herranz-Herruzo, A. Valero-Nogueira, and B. Bernardo-Clemente, "Performance assessment of gap-waveguide array antennas: CNC milling versus three-dimensional printing," *IEEE Antennas Wireless Propag. Lett.*, vol. 17, no. 11, pp. 2056–2060, Nov. 2018.
[23] A. Tamayo-Dominguez, J.-M. Fernandez-Gonzalez, and M. Sierra-Castaner, "3-D-printed modified butler matrix based on gap waveguide at W-band for monopulse radar," *IEEE Trans. Microw. Theory Techn.*, vol. 68, no. 3, pp. 926–938, Mar. 2020.
[24] M. Sierra-Castaner, M. Sierra-Perez, M. Vera-Isasa, and J. L. Fernandez-Jambrina, "Low-cost monopulse radial line slot antenna," *IEEE Trans. Antennas Propag.*, vol. 51, no. 2, pp. 256–263, Feb. 2003.
[25] J. L. Vazquez-Roy, A. Tamayo-Dominguez, E. Rajo-Iglesias, and M. Sierra-Castaner, "Radial line slot antenna design with groove gap waveguide feed for monopulse radar systems," *IEEE Trans. Antennas Propag.*, vol. 67, no. 10, pp. 6317–6324, Oct. 2019.
[26] A. Tamayo-Dominguez, J.-M. Fernandez-Gonzalez, and M. S. Castaner, "Low-cost millimeter-wave antenna with simultaneous sum and difference patterns for 5G Point-to-Point communications," *IEEE Commun. Mag.*, vol. 56, no. 7, pp. 28–34, Jul. 2018.
[27] H. Moody, "The systematic design of the butler matrix," *IEEE Trans. Antennas Propag.*, vol. 12, no. 6, pp. 786–788, Nov. 1964.
[28] A. Berenguer, V. Fusco, D. E. Zelenchuk, D. Sanchez-Escuderos, M. Baquero-Escudero, and V. E. Boria-Esbert, "Propagation characteristics of groove gap waveguide below and above cutoff," *IEEE Trans. Microw. Theory Techn.*, vol. 64, no. 1, pp. 27–36, Jan. 2016.
[29] M. Sierra-Castañer, M. Sierra-Pérez, M. Vera-Isasa, and J. L. Fernández-Jambrina, "Fast analysis model for radial-line slot antennas," *Microw. Opt. Technol. Lett.*, vol. 44, no. 1, pp. 17–21, Jan. 2005.
[30] D. M. Pozar, *Microwave Engineering*. New York, NY, USA: Wiley, 1998.
[31] *Accura SL 5530 High Temperature Resistant Stereolithography Material*. Accessed: Oct. 9, 2020. [Online]. Available: www.3dsystems.com/sites/default/files/2017-11/3d-systems-accura-sl-5530-datasheet-usen-2017-11-08-web.pdf

Adrián Tamayo-Domínguez (Student Member, IEEE) was born in Madrid, Spain, in 1991. He received the M.Sc. degree in telecommunication engineering and the Ph.D. degree from the Universidad Politécnica de Madrid, Madrid, Spain, in 2016 and 2020, respectively.

Since 2020, he is an Assistant Professor at Universidad Politécnica de Madrid. His current research interests are RF circuits, gap waveguides, and higher symmetries applied on planar antenna applications.

José-Manuel Fernández-González (Senior Member, IEEE) was born in Lausanne, Switzerland. He received the Diplôme d'Ingénieur en Électricité degree from the École Polytechnique Fédérale de Lausanne (EPFL), Lausanne, Switzerland, in 2003, and the Ph.D. degree from the Universidad Politécnica de Madrid, Madrid, Spain, in 2009.

Since 2013, he is an Assistant Professor at Universidad Politécnica de Madrid and his current research interest is phased array antennas, RF circuits, and metamaterial structures with emphasis on planar antenna applications.

Manuel Sierra-Castañer (Senior Member, IEEE) was born in Zaragoza, Spain, in 1970.

Since 1998, he has worked at the Technical University of Madrid, Madrid, Spain, from Research Assistant to Full Professor. His current research interests involve planar antennas and antenna measurement systems.

Mr. Sierra-Castañer obtained the IEEE Antennas and Propagation Symposium (APS) 2007 Schelkunoff Prize for his paper "Dual-Polarization Dual-Coverage Reflect Array for Space Applications."